18th International Conference on Information Fusion
Washington, DC - July 6-9, 2015

Bayesian Passive Sonar Tracking with Conventional Beamformer-Level Data

Ryan J. Pirkl and Jason M. Aughenbaugh
Applied Research Laboratories
The University of Texas at Austin
Austin, TX 78713-8029
Email: {rpirkl, jason}@arlut.utexas.edu

***Abstract*—A likelihood function for a multi-sensor, passive sonar Bayesian tracker may use data directly from the array elements or, alternatively, from the output of a conventional beamformer (CBF). Here, we compare the performance of a Bayesian tracker when using element- versus CBF-level data. We observed that, provided the CBF's beams are sufficiently closely spaced, the tracker's performance with CBF-level data is similar to when it is using element-level data. However, when the spacing between CBF beams becomes too large, tracker performance with CBF-level data degrades significantly, particularly when the target is located between the maximum response axes of two adjacent beams.**

I. Introduction

Bayesian trackers integrate measurements by way of a likelihood function describing the likelihood of the observed measurement given that a target is in a particular state [1]. For passive sonars, the likelihood function is ideally derived based on the statistics of the raw signals observed at the outputs of the array elements [2], [3]. For a single signal of interest, this allows the likelihood function to implicitly leverage the interference and noise rejection capabilities of adaptive beamforming techniques such as minimum variance distortionless response (MVDR) beamforming [4]–[6].

However, some passive sonar receivers may provide access only to the output signals of a conventional beamformer (CBF). As compared to element-level data, CBF-level data is much simpler to analyze due to its explicit dependence on bearing. Furthermore, when the number of CBF beams is less than the number of array elements, conventional beamforming provides a form of data compression that relaxes system requirements for data storage and data processing.

One approach to handling CBF-level data is to formulate a likelihood function based on the signals' power (i.e., magnitude-squared) statistics [7]. This is not optimal however, as it neglects the phase-dependent covariances between signals from different beams. Here, we present a passive sonar single-signal log-likelihood ratio (SSLLR) based on the statistics of the raw outputs of the CBF. This new formulation enables Bayesian passive sonar tracking with CBF-level passive sonar data and inherently provides interference and noise rejection via MVDR beamforming of the CBF-level data as in [8], [9]. We demonstrate by use of simulations that CBF-level data and element-level data lead to comparable performance of a 2-D Cartesian-based position-velocity Bayesian tracker provided that a sufficient number of CBF beams are used.

We begin by describing the signal model in Section II. SSLLRs for element- and CBF-level data are presented in Section III. Section IV describes the process for estimating various signal and noise parameters required to use the SSLLRs. In Section V, we compare the performance of a Bayesian tracker when using either the element- or CBF-level SSLLR. Conclusions are presented in Section VI.

II. Signal Model

A. Element-Level Signals

For a single frequency f, the kth T-second snapshot of the output of an N element array of omnidirectional sensors in the presence of $M+1$ uncorrelated sources and ambient noise may be described by an N-element column vector $\mathbf{x}$ given by

$$\mathbf{x}_k = \sum_{m=0}^{M} s_{k,m}\mathbf{v}(\phi_m) + \mathbf{n}_k, \tag{1}$$

where $s_{k,m}$ is the signal due to the mth source during snapshot k, $\mathbf{v}$ is the array steering vector, ϕ_m denotes the direction of arrival of the mth source's signal in azimuth during snapshot k and $\mathbf{n}_k$ is the ambient noise during snapshot k. Here, $k \in \{1, 2, \cdots, K\}$, $m \in \{0, 1, \cdots, M\}$. For simplicity, we assume that ϕ_m is effectively constant over K snapshots. We also assume all sources are in the far-field of the array whereby the signals impinging on the array may be modeled as plane waves. The array steering vector is an N-element column vector given by

$$\mathbf{v}(\phi) = \begin{bmatrix} e^{j\mathbf{k}(\phi)\cdot\mathbf{r}_1} & \cdots & e^{j\mathbf{k}(\phi)\cdot\mathbf{r}_N} \end{bmatrix}^T \tag{2}$$

for some direction of arrival ϕ. In (2), $\mathbf{r}_n$, $n \in \{1, 2, \cdots, N\}$ denotes the position of the nth array element, and $\mathbf{k}$ is the wavevector given by

$$\mathbf{k}(\phi) = \frac{2\pi f}{c}\hat{\mathbf{k}}(\phi), \tag{3}$$

where c is the speed of sound and $\hat{\mathbf{k}}(\phi)$ is a unit vector in the direction ϕ.

The element-level sample covariance matrix is

$$\mathbf{C}_\mathbf{x} = \frac{1}{K}\sum_{k=1}^{K}\mathbf{x}_k\mathbf{x}_k^H, \tag{4}$$

whereby the covariance matrix is estimated from K snapshots and $(\cdot)^H$ denotes the conjugate transpose. In practice, K_t snapshots may be taken at K_f closely-spaced frequencies such that $K = K_t K_f$, provided that $T/8K_f$ is less than the transit time of the array and the target may be approximated as stationary in bearing for duration $K_t T$ [10].

We assume $s_{k,m}$ and $\mathbf{n}_k$ for all k, m may be described by uncorrelated circular complex Gaussian random processes that are wide-sense stationary over the K snapshots. Then, the covariance matrix of $\mathbf{x}_k$ is

$$\mathbf{R}_{\mathbf{x}}(\mathbf{s}) = E\{\mathbf{x}_k \mathbf{x}_k^H\} = \sum_{m=0}^{M} \sigma_m^2 \mathbf{v}(\phi_m)\mathbf{v}^H(\phi_m) + \mathbf{R}_{\mathbf{n}}, \quad (5)$$

where σ_m^2 is the variance of the mth source's signal and $\mathbf{R}_{\mathbf{n}}$ is the covariance matrix of the noise $\mathbf{n}_k$ as given by

$$\mathbf{R}_{\mathbf{n}} = E\{\mathbf{n}_k \mathbf{n}_k^H\}, \quad (6)$$

and $\mathbf{s} = \{\sigma_m^2, \phi_m, \mathbf{R}_{\mathbf{n}}\}_{m=0}^{M}$ is the set of all considered state parameters.

B. Conventional Beamformer-Level Signals

Let us assume that the element-level outputs are processed by a CBF using L look directions ψ_ℓ. The L-element output vector for the CBF is given by

$$\mathbf{y}_k = \mathbf{B}^H \mathbf{x}_k, \quad (7)$$

where $\mathbf{B}$ is the N-by-L matrix of weights for the CBF as given by

$$\mathbf{B} = \left[\begin{array}{ccc} \mathbf{v}(\psi_1) & \cdots & \mathbf{v}(\psi_L) \end{array} \right]. \quad (8)$$

For later use, we define the CBF-level sample covariance matrix as

$$\mathbf{C}_{\mathbf{y}} = \frac{1}{K} \sum_{k=1}^{K} \mathbf{y}_k \mathbf{y}_k^H \quad (9)$$

and the CBF-level array steering vector as

$$\tilde{\mathbf{v}}(\phi) = \mathbf{B}^H \mathbf{v}(\phi). \quad (10)$$

III. Single-Signal Log-Likelihood Ratio

We consider the SSLLR as described in [4], [11], which marginalizes the log-likelihood ratio from a dependence on all state parameters $\mathbf{s}$ to a dependence solely on the bearing of the signal-of-interest. We assume that the m'th source is the signal-of-interest, whereby the other M sources ($m \neq m'$) are effectively interferers.

A. Element-Level Single-Signal Log-Likelihood Ratio

For element-level signals, the SSLLR for the m'th signal is

$$\log L_{m'}(\mathbf{X}|\phi_{m'}) = K \left[-\log\left(1 + \frac{\sigma_{m'}^2}{\nu(\phi_{m'})}\right) + \left(\frac{\frac{\sigma_{m'}^2}{\nu(\phi_{m'})}}{1 + \frac{\sigma_{m'}^2}{\nu(\phi_{m'})}} \right) \frac{P(\phi_{m'})}{\nu(\phi_{m'})} \right] \quad (11)$$

as shown in [4], [11], where $\mathbf{X} = \{\mathbf{x}_k\}_{k=1}^{K}$ is the set of K element-level snapshots, $P_{m'}(\phi)$ is the MVDR beamformer's received power versus look angle as given by

$$P_{m'}(\phi) = \mathbf{w}_{m'}^H(\phi) \mathbf{C}_{\mathbf{x}} \mathbf{w}_{m'}(\phi) \quad (12)$$

and $\nu_{m'}(\phi)$ is the average received noise-plus-interference versus look angle as given by

$$\nu_{m'}(\phi) = \mathbf{w}_{m'}^H(\phi) \mathbf{R}_{n+i,m'} \mathbf{w}_{m'}(\phi). \quad (13)$$

In (12) and (13), $\mathbf{w}_{m'}$ is the MVDR beamformer's weights given by

$$\mathbf{w}_{m'}(\phi) = \frac{\mathbf{R}_{n+i,m'}^{-1}(\mathbf{s})\mathbf{v}(\phi)}{\mathbf{v}(\phi)^H \mathbf{R}_{n+i,m'}^{-1}(\mathbf{s})\mathbf{v}(\phi)} \quad (14)$$

and $\mathbf{R}_{n+i,m'}(\mathbf{s})$ in (12)-(14) is the combined noise-plus-interference covariance matrix given by

$$\mathbf{R}_{n+i,m'}(\mathbf{s}) = \sum_{\substack{m=0 \\ m \neq m'}}^{M} \sigma_m^2 \mathbf{v}(\phi_m)\mathbf{v}^H(\phi_m) + \mathbf{R}_{\mathbf{n}}, \quad (15)$$

which is similar to (5) except that the summation excludes the signal of interest corresponding to $m = m'$

Observe that the SSLLR is formulated under the assumption that the noise-plus-interference covariance matrix $\mathbf{R}_{n+i,m'}(\mathbf{s})$ and the m'th source's signal power $\sigma_{m'}^2$ are known or may be estimated from the measurement data. Then, the SSLLR depends only on the signal-of-interest's direction-of-arrival $\phi_{m'}$. The estimation of $\mathbf{R}_{n+i,m'}(\mathbf{s})$ and $\sigma_{m'}^2$ shall be addressed in Section IV.

B. CBF-Level Single-Signal Log-Likelihood Ratio

It may be shown that the SSLLR for CBF-level signals takes a form similar to that presented in (11):

$$\log L_{m'}(\mathbf{Y}|\phi_{m'}) = K \left[-\log\left(1 + \frac{\sigma_{m'}^2}{\tilde{\nu}(\phi_{m'})}\right) + \left(\frac{\frac{\sigma_{m'}^2}{\tilde{\nu}(\phi_{m'})}}{1 + \frac{\sigma_{m'}^2}{\tilde{\nu}(\phi_{m'})}} \right) \frac{\tilde{P}(\phi_{m'})}{\tilde{\nu}(\phi_{m'})} \right] \quad (16)$$

where $\mathbf{Y} = \{\mathbf{y}\}_{k=1}^{K}$ is the set of K CBF-level snapshots. In (16), $\tilde{P}_{m'}(\phi)$ is the CBF-level MVDR beamformer's output power given by

$$\tilde{P}_{m'}(\phi) = \tilde{\mathbf{w}}_{m'}^H(\phi) \mathbf{C}_{\mathbf{y}} \tilde{\mathbf{w}}_{m'} \quad (17)$$

and $\tilde{\nu}_{m'}(\phi)$ is the CBF-level noise-plus-interference given by

$$\tilde{\nu}_{m'}(\phi) = \tilde{\mathbf{w}}_{m'}^H(\phi) \tilde{\mathbf{R}}_{n+i,m'}(\mathbf{s}) \tilde{\mathbf{w}}_{m'}(\phi). \quad (18)$$

In (17) and (18), $\tilde{\mathbf{w}}_{m'}$ is the CBF-level MVDR beamformer weights as given by

$$\tilde{\mathbf{w}}_{m'}(\phi) = \frac{\tilde{\mathbf{R}}_{n+i,m'}^{-1}(\mathbf{s})\tilde{\mathbf{v}}(\phi)}{\tilde{\mathbf{v}}(\phi)^H \tilde{\mathbf{R}}_{n+i,m'}^{-1}(\mathbf{s})\tilde{\mathbf{v}}(\phi)}. \quad (19)$$

In (18) and (19), $\tilde{\mathbf{R}}_{n+i,m'}(\mathbf{s})$ is the CBF-level noise-plus-interference covariance matrix as given by

$$\tilde{\mathbf{R}}_{n+i,m'}(\mathbf{s}) = \mathbf{B}^H \mathbf{R}_{n+i,m'}(\mathbf{s}) \mathbf{B}. \quad (20)$$

IV. Estimation of the Signal and Noise Parameters

As indicated by (15), computation of $\mathbf{R}_{n+i,m'}(\mathbf{s})$ [or $\tilde{\mathbf{R}}_{n+i,m'}(\mathbf{s})$ by way of (20)] requires knowledge of the interfering sources' parameters ϕ_m and σ_m^2 for $m \neq m'$, the noise covariance matrix $\mathbf{R}_n$, and the signal-of-interest's power $\sigma_{m'}^2$. The following sections describe our approach to estimating these parameters. For brevity, we limit our discussion to signal power and noise estimates for element-level data. As may be deduced from Sections III, the corresponding parameter estimates for beam-level data may be determined by making the following substitutions in the text and equations: $L \rightarrow N$, $\mathbf{C_y} \rightarrow \mathbf{C_x}$, $\tilde{\mathbf{v}}(\phi) \rightarrow \mathbf{v}(\phi)$, $\mathbf{B}^H\mathbf{R_n}\mathbf{B} \rightarrow \mathbf{R_n}$, and $\mathbf{B}^H\mathbf{R}_{\text{iso}}\mathbf{B} \rightarrow \mathbf{R}_{\text{iso}}$, where $\mathbf{R}_{\text{iso}}$ is the element-level covariance matrix for isotropic noise as discussed in Section IV-A.

A. Noise Estimation

We assume the underwater ambient noise is isotropic such that the element-level noise covariance matrix is given by

$$\mathbf{R_n} = \sigma_{\mathbf{n}}^2 \mathbf{R}_{\text{iso}}, \tag{21}$$

where $\sigma_{\mathbf{n}}^2$ is the noise power at each array element and $\mathbf{R}_{\text{iso}}$ describes the covariance between array elements due to unit power isotropic ambient noise; see [12] for guidance on computing $\mathbf{R}_{\text{iso}}$. In [11], the noise was assumed spatially white such that the noise covariance matrix was assumed proportional to an identity matrix. This enabled a simple computation of the maximum likelihood noise power estimate [11]. Although the formulation may be adapted to isotropic noise, we have found it to be unreliable due to the potentially ill-conditioned nature of $\mathbf{R}_{\text{iso}}$, particularly when the array is operated at a frequency well below its design frequency. We thus use an alternative noise estimate that is based on the solution to the following minimization problem:

$$\min_{\hat{\sigma}_n^2} \left\| \mathbf{C_x} - \left[\sum_{m=0}^{M} \hat{\sigma}_m^2 \mathbf{v}(\hat{\phi}_m)\mathbf{v}^H(\hat{\phi}_m) + \hat{\sigma}_{\mathbf{n}}^2 \mathbf{R}_{\text{iso}} \right] \right\|^2, \tag{22}$$

where $\|\cdot\|$ denotes the Frobenius norm. Equation (22) finds the noise power estimate such that the modeled covariance matrix, given by $\sum_{m=0}^{M} \hat{\sigma}_m^2 \mathbf{v}(\hat{\phi}_m)\mathbf{v}^H(\hat{\phi}_m) + \hat{\sigma}_{\mathbf{n}}^2 \mathbf{R}_{\text{iso}}$, is closest to the sample covariance matrix $\mathbf{C_x}$ in the Frobenius norm. In (22), $\hat{\phi}_m$ and $\hat{\sigma}_m^2$ denote direction-of-arrival estimates and source power estimates, respectively.

Defining

$$\mathbf{C_n} = \mathbf{C_x} - \sum_{m=0}^{M} \hat{\sigma}_m^2 \mathbf{v}(\hat{\phi}_m)\mathbf{v}^H(\hat{\phi}_m) \tag{23}$$

as the nominally noise-only sample covariance matrix, (22) becomes

$$\min_{\sigma_{\mathbf{n}}^2} \left\| \mathbf{C_n} - \hat{\sigma}_{\mathbf{n}}^2 \mathbf{R}_{\text{iso}} \right\|^2. \tag{24}$$

The solution to (24) is

$$\hat{\sigma}_{\mathbf{n}}^2 = \frac{\text{tr}\left(\mathbf{V}^{-1}\mathbf{C_n}\mathbf{V}\mathbf{D}\right)}{\text{tr}\left(\mathbf{D}^2\right)}, \tag{25}$$

where the columns of $\mathbf{V}$ are the eigenvectors of $\mathbf{R}_{\text{iso}}$ and $\mathbf{D}$ is a diagonal matrix whose elements are the corresponding real eigenvalues d_n such that

$$\mathbf{R}_{\text{iso}} = \mathbf{V}\mathbf{D}\mathbf{V}^{-1}, \tag{26}$$

and $\text{tr}(\cdot)$ denotes the matrix trace. Using the matrix trace, (25) may be rewritten as

$$\hat{\sigma}_{\mathbf{n}}^2 = \frac{\sum_{n=1}^{N} (c_n/d_n)|d_n|^2}{\sum_{n=1}^{N} |d_n|^2}, \tag{27}$$

where c_n is the nth diagonal element of $\mathbf{V}^{-1}\mathbf{C_n}\mathbf{V}$.

Equation (27) shows that $\hat{\sigma}_{\mathbf{n}}^2$ is a *weighted* average of the ratio c_n/d_n. The weighting $|d_n|^2$ makes $\hat{\sigma}_{\mathbf{n}}^2$ robust when the ratio's denominator d_n approaches zero. However, it also tends to skew the estimate towards values of c_n/d_n where $|d_n|$ is large. Through numerical simulations, we have found that (27) tends to underestimate the noise power, leading to false detections. We have addressed this problem by making two modifications to the formulation. First, we force $\mathbf{C_n}$ to be positive semidefinite. This is achieved by zeroing out any negative eigenvalues of $\mathbf{C_n}$ as defined in (23). Second, assuming d_n composing $\mathbf{D}$ are sorted from greatest to least such that $d_{n-1} \geq d_n$ for all $n \in \{0, 1, \cdots N\}$, we estimate the noise power by way of an *unweighted* average of the first N' ratios c_n/d_n:

$$\hat{\sigma}_{\mathbf{n}}^2 = \frac{1}{N'} \sum_{n=1}^{N'} c_n/d_n. \tag{28}$$

The truncation point N' is determined by the number of significant eigenvalues d_n. Specifying r as the rank of $\mathbf{R_n}$, we determine the truncation point as

$$N' = \max N' \text{ s.t. } \sum_{n=0}^{N'} |d_n| \leq \left(1 - \frac{1}{10r}\right) \sum_{n=0}^{r} |d_n|. \tag{29}$$

For example, if $\mathbf{R_n}$ had a rank of $r = 10$, N' is chosen such that the first N' eigenvalues contain approximately 99 % of the power in $\mathbf{R_n}$.

B. Signal Parameter Estimation

We use maximum likelihood estimates $\hat{\sigma}_{m'}^2$ and $\hat{\phi}_{m'}$ for the signal power and direction-of-arrival, respectively, of the m'th source as done in [11]. The estimates are given by the solutions to

$$\{\hat{\sigma}_{m'}^2, \hat{\phi}_{m'}\} = \underset{\hat{\sigma}_{m'}^2, \hat{\phi}_{m'}}{\arg\max} \log L_{m'}(\mathbf{X}|\hat{\phi}_{m'}) \tag{30}$$

for all $m' \in \{0, 1, 2, \ldots, M\}$ with the constraint that $\sigma_{m'}^2 \geq 0$. Due to the dependence of Equation (30)'s parameter estimates for the m'th source on the parameter estimates for all other sources, (30) must be solved iteratively, with each iteration including a refinement of the noise power estimate in (28).

C. Iterative Refinement of Estimates

Following [4], the iterative estimation procedure is initialized by first assuming that one source was present ($M = 0$). The mean of the $N - M - 1$ smallest eigenvalues of $\mathbf{C_x}$ is used as the noise estimate. Then, the signal parameters of the $M + 1$ sources are estimated followed by a new noise estimate using (29). The signal and noise estimation step is then repeated until the estimates converge. The assumed number of sources is then incremented (i.e., $M = 1$), a new initial noise estimate is computed, and the signal parameter estimates and noise estimates are again iteratively refined. This procedure is repeated until the assumed number of sources equals the actual number of sources, which must be known *a priori* or else postulated from the measurements.

Once all parameters have been determined, the signal-of-interest's direction-of-arrival $\phi_{m'}$ is treated as an unknown dependent variable so as to evaluate the SSLLR in (11) for different bearings of the source-of-interest. This measurement-based likelihood function may then be combined with *a priori* estimates of the probability density function of the source-of-interest's bearing/location and a stochastic model of the source-of-interest's kinematics so as to realize a Bayesian tracker.

D. Matrix Inversion

The SSLLR requires the inversion of $\mathbf{R}_{n+i}$. Depending on the array configuration and relative signal powers, this matrix may be ill-conditioned such that its inverse is extremely susceptible to numerical error. We address this issue by use of the regularized matrix inverse appearing in Tikhonov regularization of ill-conditioned linear least-squares problems. For a matrix $\mathbf{A}$, this regularized inverse is given by (c.f. [13])

$$\hat{\mathbf{A}}^{-1} = \left(\mathbf{A}^H\mathbf{A} + \lambda\mathbf{I}\right)^{-1}\mathbf{A}^H, \tag{31}$$

where $\mathbf{I}$ is the identity matrix and λ is the scalar regularization parameter. Conventional approaches to specifying λ make use of the observation vector in an ill-conditioned linear least-squares problem; see [13]–[15] and references therein. Lacking a linear least-squares problem—we are fundamentally trying to solve for the MVDR weights, which are the solutions to a linearly constrained quadratic problem—we opt to set λ equal to the smallest "significant" singular value of $\mathbf{A}$, which we denote as s_{N_λ}. This is motivated by applying the singular value decomposition $\mathbf{A} = \mathbf{USV}^H$ to (31), which yields

$$\hat{\mathbf{A}}^{-1} = \mathbf{V}\left(\mathbf{S}^2 + \lambda^2\mathbf{I}\right)^{-1}\mathbf{SU}^H. \tag{32}$$

Comparing (32) to the pseudoinverse of $\mathbf{A}$ as given by $\mathbf{VS}^{-1}\mathbf{U}^H$, we see that λ suppresses the reciprocal of "small" singular values (i.e., those much less than λ) while negligibly perturbing "large" singular values (i.e., those much greater than λ). In a procedure analogous to that used in (29), we specify $r_{\mathbf{A}}$ as the rank of $\mathbf{A}$ and determine N_λ via

$$N_\lambda = \max N'_\lambda \text{ s.t. } \sum_{i=1}^{N_\lambda} s_i \leq \left(1 - \frac{1}{10r_{\mathbf{A}}}\right)\sum_{i=1}^{r_{\mathbf{A}}} s_i. \tag{33}$$

TABLE I
SIMULATION DETAILS

Parameter	Value
Ambient noise spectrum level	60 dB re 1 μPa^2/Hz
Target source spectrum level	123 dB re 1 μPa^2/Hz
Target source bandwidth	3 Hz
Measurement center frequency	750 Hz
Snapshot duration	$T = 0.64$ s
Frequency snapshots per measurement	$K_f = 9$
Time snapshots per measurement	$K_t = 188$
Total snapshots per measurement	$K = K_f K_t = 1692$
Measurement duration	$K_t T = 120$ s
Tracking bandwidth	$K_f/T = 14$ Hz
Array directivity	16 dB at 750 Hz

V. SIMULATIONS

The bearing-dependent SSLLRs were mapped to Cartesian space for integration into a 2-D Cartesian Bayesian tracker designed to facilitate multi-sensor data fusion. The tracker featured a 2-D Cartesian position-velocity probability density grid [16], a hybrid particle-grid motion update procedure [17], and a birth-death model for the movement of a source into or out of the tracking region [18]. Further details about the Bayesian tracker implementation may be found in [19], [20]. Although the tracker supports multi-sensor data fusion, we limit our scope to single sensor scenarios so as to compare the performance of the tracker with element-level versus CBF-level signals.

The Sonar Simulation Toolset (SST) [21] was used to generate three different underwater target detection and tracking scenarios. The simulations used a uniform circular array of $N = 50$ omnidirectional elements. The inter-element spacing was 0.75 m, which corresponds to a half-wavelength at 1 kHz. The array was positioned in the horizontal plane at a depth of 20 m. Tracking was done within an 80 km by 80 km region of interest centered about the array. The signal of interest was a narrowband signal at 750 Hz generated by a single target moving at a speed of 5 m/s within the tracking region at a constant depth of 20 m. Our immediate application of interest does not consider interferers, so no additional sources were specified. Additional simulation details are provided in Table I.

Element-level data was simulated from SST and used to compute the CBF-level data via (7). For the CBF-level data, we considered $L \in \{30, 40, 50\}$ look directions equispaced in bearing. The element- and CBF-level data were then used to compute SSLLRs. Each of the three simulation scenarios was repeated five times by generating five unique element-level data sets from SST.

A. Tracker Performance Metrics

We consider three performance metrics for the Bayesian tracker: target probability P_t, the error in the maximum *a posteriori* (MAP) of the target bearing probability density function (PDF) ϕ_{MAP}, and the angular spread of the target

bearing PDF Λ_ϕ. The target probability comes naturally from the Bayesian tracker framework and indicates the probability that a target is in the region of interest. The MAP target bearing is the maximum of the posterior of the target bearing PDF, denoted $f_\Phi(\phi)$, which is itself conditioned on a target being in the tracking region. The target bearing PDF $f_\Phi(\phi)$ is calculated by marginalizing the tracker's 2-D Cartesian target position PDF with respect to range from the array. The bearing PDF angular spread provides a measure of target localization. As shown in [22], it is computed as

$$\Lambda_\phi = \sqrt{1 - \frac{|F_1|^2}{|F_0|^2}}, \tag{34}$$

where F_n are angular Fourier coefficients calculated as

$$F_n = \int_0^{2\pi} f_\Phi(\phi) e^{jn\phi} d\phi. \tag{35}$$

The bearing PDF angular spread[1] takes on values from 0 to 1, with 0 corresponding to a highly localized target [e.g., for $f_\Phi(\phi) = \delta(\phi - \phi_0)$ where $\delta(\phi)$ is the Dirac delta function] and 1 corresponding to a poorly localized target [e.g., for $f_\Phi(\phi) = 1/(2\pi)$].

B. Simulation 1: Linear Target Path within CBF Beam

For the first scenario, the target's initial bearing and range are 0° and 30 km, respectively. The target's heading is 180° and is closing on the receiver array at a rate of 5 m/s. The L equispaced CBF beams are arranged such that the first beam's maximum response axis (MRA) is at 0°. Thus, for this scenario, the target is headed straight towards the receiver and its path lies along the MRA of the first CBF beam.

Tracker performance metrics averaged over the five simulation trials are presented in Fig. 1. We observe that the transition from $P_t \approx 0$ to $P_t \approx 1$ occurs during measurements 20–30, wherein the target range is 18–12 km, and the tracking-bandwidth-averaged spectrum level of the signal-of-interest arriving at the array is 34–30 dB re 1 μPa^2/Hz, respectively. Excepting for CBF-level data with $L = 30$, the tracker performance for CBF- and element-level data is similar. When only $L = 30$ CBF beams are used, we observe a slight degradation in the tracker's performance that is realized as a latency in the detection and localization of a target.

C. Simulation 2: Linear Target Path between CBF Beams

For the second scenario, we use the same target path that was used in the first scenario but consider a rotation of the L CBF beams by π/L such that 0° in bearing lies *between* the maximum response axes of the CBF's first and second beams. As compared to scenario #1, this "between CBF beams" configuration is expected to result in a consistently lower target signal-to-noise ratio (SNR) such that detection and localization of the target does not occur until the target is closer to the receiver. For this rotated beam configuration, we note that the first and second beams' scalloping loss in the direction of the target (0°) for $L = 50$, 40, and 30 is 3.2 dB, 5.5 dB, and 12.2 dB, respectively. For convenience and to facilitate comparisons to scenario #1, we use the element-level data from scenario #1's five trials to compute the CBF-level data for the rotated CBF beams. Therefore, the corresponding element-level results for scenario #2 are identical to those in scenario #1.

Figure 2 presents the tracker performance metrics for the rotated CBF beams averaged over the five trials. For the between-beam configuration, we observe a much greater latency in the target detection and localization when using $L = 30$ CBF beams as compared to scenario #1's within-beam configuration. This is attributed to the 12.2 dB reduction in SNR due to the beams' scalloping loss in the direction of the target. For $L = \{50, 40\}$, we observe a very small degradation in tracker performance, with $L = 50$ performing slightly better than $L = 40$. This behavior was found to be consistent across all five trials.

D. Simulation 3: Spiral Target Path

For the third scenario, the target slowly approaches the receiver array along the spiral path shown in Fig. 3. The target maintains a constant speed of 5 m/s. We use the non-rotated CBF beam arrangement from scenario #1 where the first beam's MRA is at 0°.

Figure 4 compares the trial-averaged tracker performance for the different configurations. We observe that the transition from $P_t \approx 0$ to $P_t \approx 1$ occurs during measurements 60–90, wherein the target range is 18–14 km, and the tracking-bandwidth-averaged spectrum level of the signal-of-interest arriving at the array is 34–32 dB re 1 μPa^2/Hz, respectively. Similar to scenario #2, we observe a significant degradation in target detection and localization with $L = 30$ as compared to the element-level data configuration. In contrast to scenario #2, we observe that CBF-level data with $L = 40$ shows slightly better performance than $L = 50$ during the time in which the target is becoming detectable, roughly measurements 70–85. Examining the per-trial results, we have found that for the fifth trial, $L = 40$ demonstrated better performance than $L = 50$. However, for all other trials, the performance of $L = 40$ and $L = 50$ were nearly identical. Thus, we do not consider the differences in performance between $L = 50$ and $L = 40$ in Fig. 4 to be significant. Additional trials are needed to confirm this.

VI. Conclusions

Using CBF-level data with $L < N$ can be desirable when one wants to reduce the data storage and/or throughput requirements for a target tracker. Here, we have shown that tracking performance when using element- versus CBF-level data can be comparable provided that a sufficient number of CBF beams are used. For the tracking scenarios, array geometry, and measurement frequency considered here, we observed the tracking performance for an $N = 50$ element uniform circular

[1] Angular spread as defined by (34)-(35) was originally conceived as a measure of how incident power is spread in azimuth; that is, the width of a power-angle spectrum. We have found it equally useful for quantifying the width of a bearing-dependent PDF.

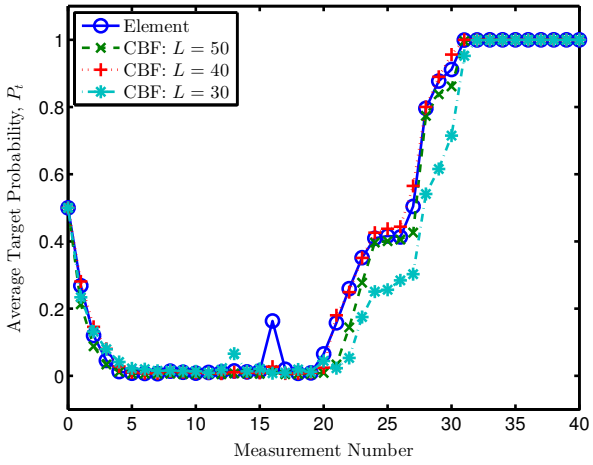

(a) Average target probability

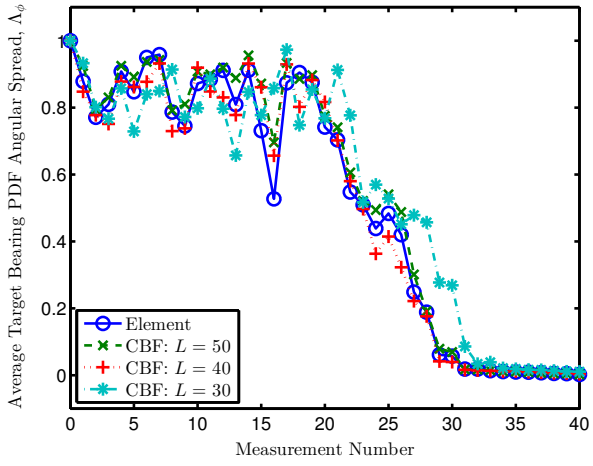

(b) Average target bearing angular spread

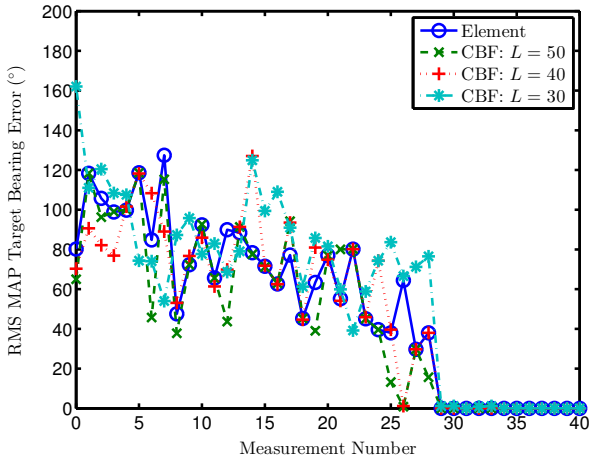

(c) RMS MAP target bearing error

Fig. 1. Tracker performance metrics averaged over five runs for the linear target path within a CBF beam.

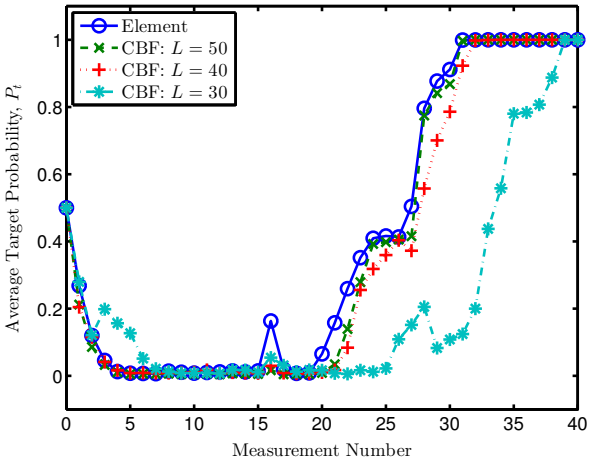

(a) Average target probability

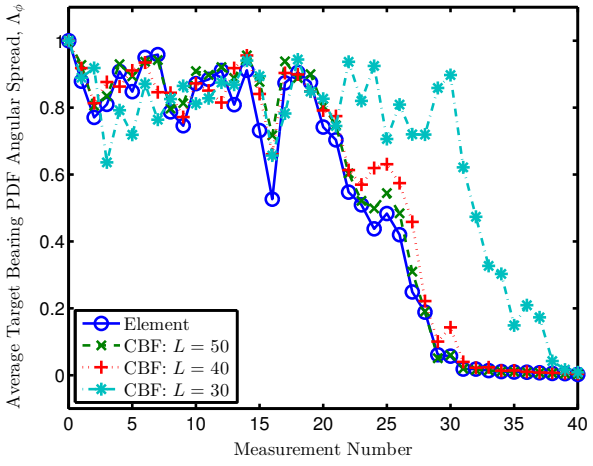

(b) Average target bearing angular spread

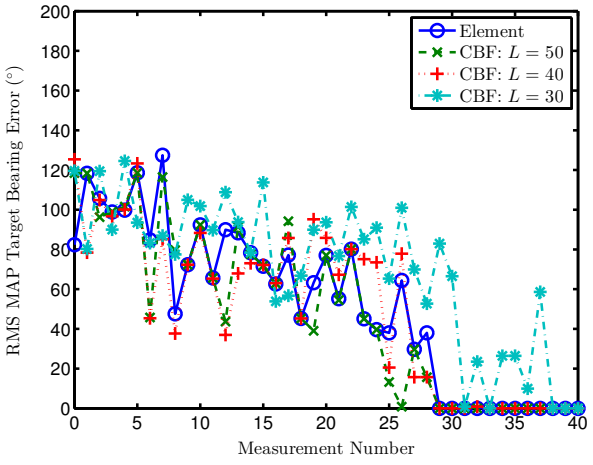

(c) RMS MAP target bearing error

Fig. 2. Tracker performance metrics averaged over five runs for the linear target path between CBF beams.

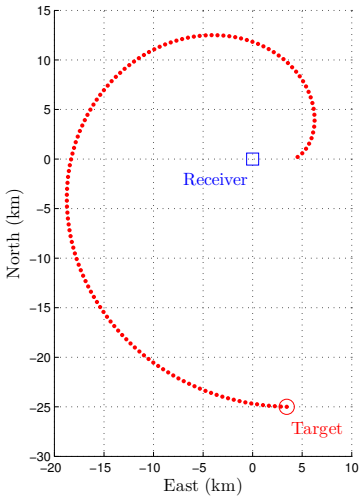

Fig. 3. Spiral path of the target used in Simulation 3. The receiver position is marked by the square. The target's initial position is marked by the circle, and its position at each measurement is marked by dots.

array was comparable when using element-level data directly versus using CBF-level data with $L \in \{50, 40\}$ equispaced CBF beams; a significant degradation in tracker performance was observed when using $L = 30$ beams.

In [8], it was shown that one should choose the number of CBF beams L such that the CBF-level covariance matrix $\mathbf{R_y}$ is full-rank for L beams and rank-deficient for $L + 1$ beams so as to maximize the SNR of the adaptively beamformed CBF-level data. This in turn may be expected to maximize the tracker's performance with CBF-level data. While theoretically sound, this guidance for choosing L can be of limited utility in practice, because the distinction between a full-rank albeit ill-conditioned $\mathbf{R_y}$ and a truly rank-deficient $\mathbf{R_y}$ is rarely clear and depends on the actual signals at the array elements.

An alternative approach to choosing L would be to consider the between-beams scalloping loss. Increased scalloping loss will reduce the SNR of the CBF-level data, which will in turn reduce the maximum achievable SNR of the adaptively beamformed CBF-level data and degrade the detection and localization performance of the tracker. Between-beam scalloping loss depends on a combination of the number of beams L, their arrangement in bearing space, the measurement frequency, and even the array geometry. Based on the simulations presented here, as well as additional simulations at 500 Hz and 1 kHz, tracker performance with CBF-level data is expected to be comparable to performance with element-level data provided that the number of beams L and their arrangement are chosen such that the between-beam scalloping loss does not exceed 6 dB.

ACKNOWLEDGMENT

This work was supported by the Office of Naval Research under contract no. N00014-11-G-0041-19.

REFERENCES

[1] L. D. Stone, C. A. Barlow, and T. L. Corwin, *Bayesian multiple target tracking*. Artech House, Inc., 1999.

[2] R. E. Bethel and K. L. Bell, "A MLE approach to joint array detection and direction of arrival estimation," in *Proc. Sensor Array and Multichannel Signal Processing Workshop*, 4–6 August 2002, pp. 169–173.

[3] C. Kreucher and B. Shapo, "Multitarget detection and tracking using multisensor passive acoustic data," *IEEE J. Ocean. Eng.*, vol. 36, no. 2, pp. 205–218, April 2011.

[4] B. A. Yocom, B. R. La Cour, and T. W. Yudichak, "A Bayesian approach to passive sonar detection and tracking in the presence of interferers," *IEEE J. Ocean. Eng.*, vol. 36, no. 3, pp. 386–405, July 2011.

[5] J. Capon, "High-resolution frequency-wavenumber spectrum analysis," *Proc. IEEE*, vol. 57, no. 8, pp. 1408–1418, August 1969.

[6] H. L. Van Trees, *Optimum Array Processing. Part IV of Detection, Estimation, and Modulation Theory*. John Wiley & Sons, Inc., 2002.

[7] B. Shapo and R. Bethel, "An overview of the probability density function (PDF) tracker," in *OCEANS 2006*, 18–21 September 2006, pp. 1–6.

[8] D. A. Gray, "Formulation of the maximum signal-to-noise ratio array processor in beam space," *J. Acoust. Soc. Am.*, vol. 72, no. 4, pp. 1195–1201, October 1982.

[9] S. D. Somasundaram, "Reduced dimension robust Capon beamformer for large aperture passive sonar," *IET Radar Sonar Navig*, vol. 5, no. 7, pp. 707–715, 2011.

[10] H. Song, W. A. Kuperman, W. S. Hodgkiss, P. Gerstoft, and J. S. Kim, "Null broadening with snapshot-deficient covariance matrices in passive sonar," *IEEE J. Ocean. Eng.*, vol. 28, no. 2, pp. 250–261, April 2003.

[11] B. A. Yocom, "Bayesian passive sonar tracking in the context of active-passive data fusion," Master's thesis, The University of Texas at Austin, August 2009.

[12] H. Cox, "Spatial correlation in arbitrary noise fields with application to ambient sea noise," *J. Acoust. Soc. Am.*, vol. 54, no. 5, pp. 1289–1301, November 1973.

[13] D. Calvetti and L. Reichel, "Tikhonov regularization of large linear problems," *BIT Numerical Mathematics*, vol. 463, pp. 263–283, 2003.

[14] S. Pereverzev and E. Schock, "On the adaptive selection of the parameter in regularization of ill-posed problems," *SIAM J. Numer. Anal.*, vol. 43, no. 5, pp. 2060–2076, 2005.

[15] H. G. Choi, A. N. Thite, and D. J. Thompson, "Comparison of methods for parameter selection in Tikhonov regularization with application to inverse force determination," *J. Sound and Vibration*, vol. 304, no. 3–5, pp. 894–917, July 2007.

[16] J. M. Aughenbaugh and B. R. La Cour, "Measurement-guided likelihood sampling for grid-based Bayesian tracking," *J. Adv. Inf. Fusion*, vol. 5, no. 2, pp. 108–127, 2010.

[17] ——, "Particle-inspired motion updates for grid-based Bayesian trackers," in *Information Fusion, 14th Int. Conf. on*, 5–8 July 2011, pp. 1–8.

[18] B. R. La Cour, "Stationary priors for Bayesian target tracking," in *Information Fusion, 11th Int. Conf. on*, 30 June–3 July 2008, pp. 1–6.

[19] B. A. Yocom, J. M. Aughenbaugh, and B. R. La Cour, "Range-sensitive Bayesian passive sonar tracking," in *Information Fusion, 13th Int. Conf. on*, 26–29 July 2010, pp. 1–10.

[20] J. M. Aughenbaugh and B. R. La Cour, "Computationally efficient Bayesian tracking," in *SPIE Defense, Security, and Sensing*, 25–26 April 2012.

[21] R. P. Goddard, "The Sonar Simulation Toolset, Release 4.6: Science, Mathematics, and Algorithms," Applied Physics Laboratory, University of Washington, Tech. Rep. APL-UW TR 0702, October 2008.

[22] G. D. Durgin and T. S. Rappaport, "Basic relationship between multipath angular spread and narrowband fading in wireless channels," *Electronics Letters*, vol. 34, no. 25, pp. 2431–2432, December 1998.

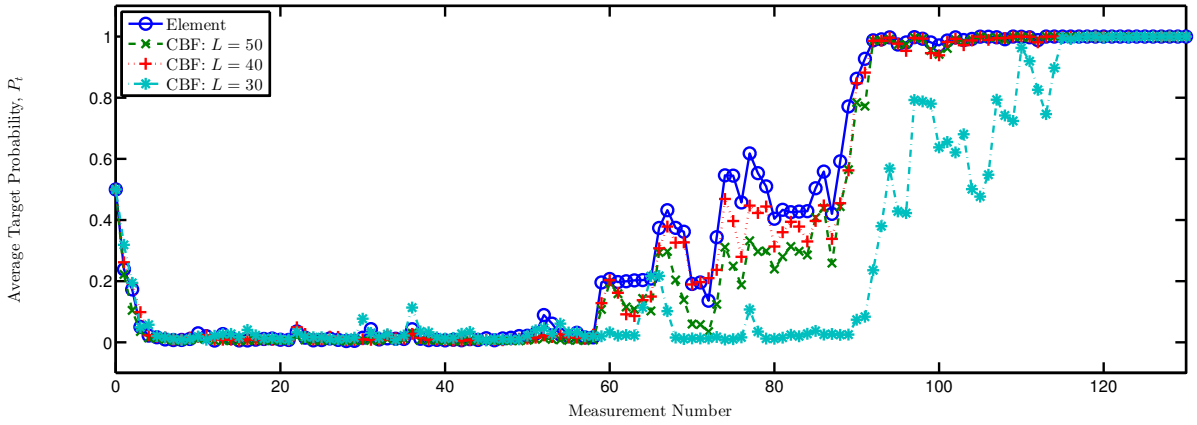

(a) Average target probability

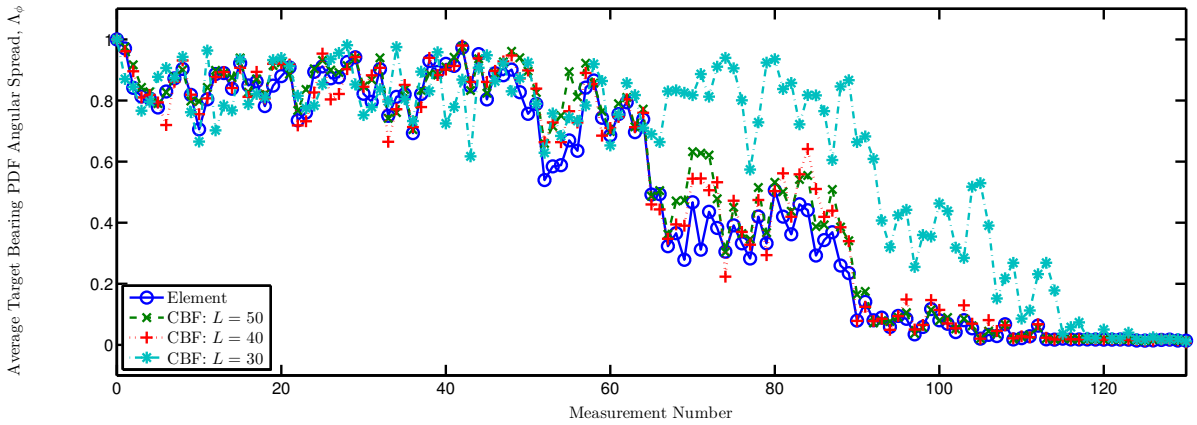

(b) Average target bearing angular spread

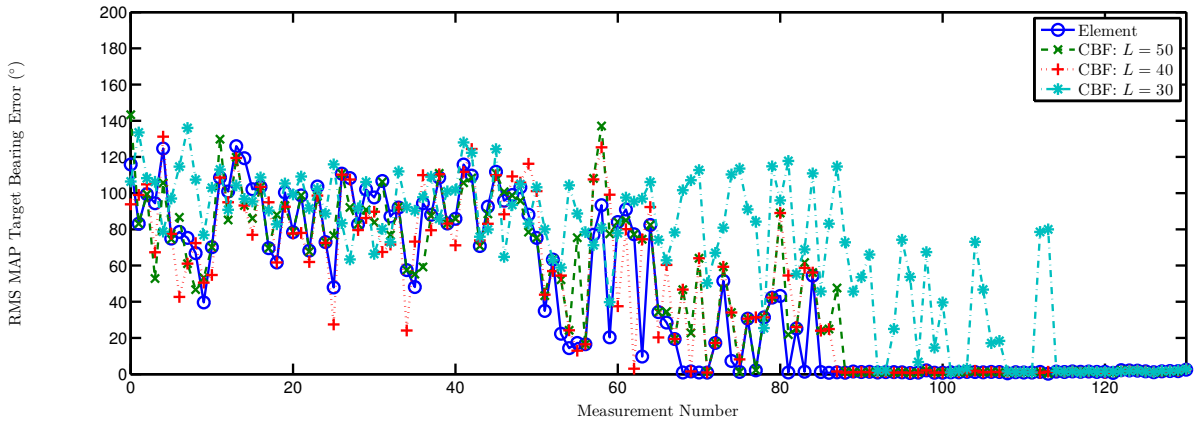

(c) RMS MAP target bearing error

Fig. 4. Tracker performance metrics averaged over five runs for the spiral target path.